May 26, 2021
Volume 143
Number 20
pubs.acs.org/JACS

JACS

JOURNAL OF THE AMERICAN CHEMICAL SOCIETY

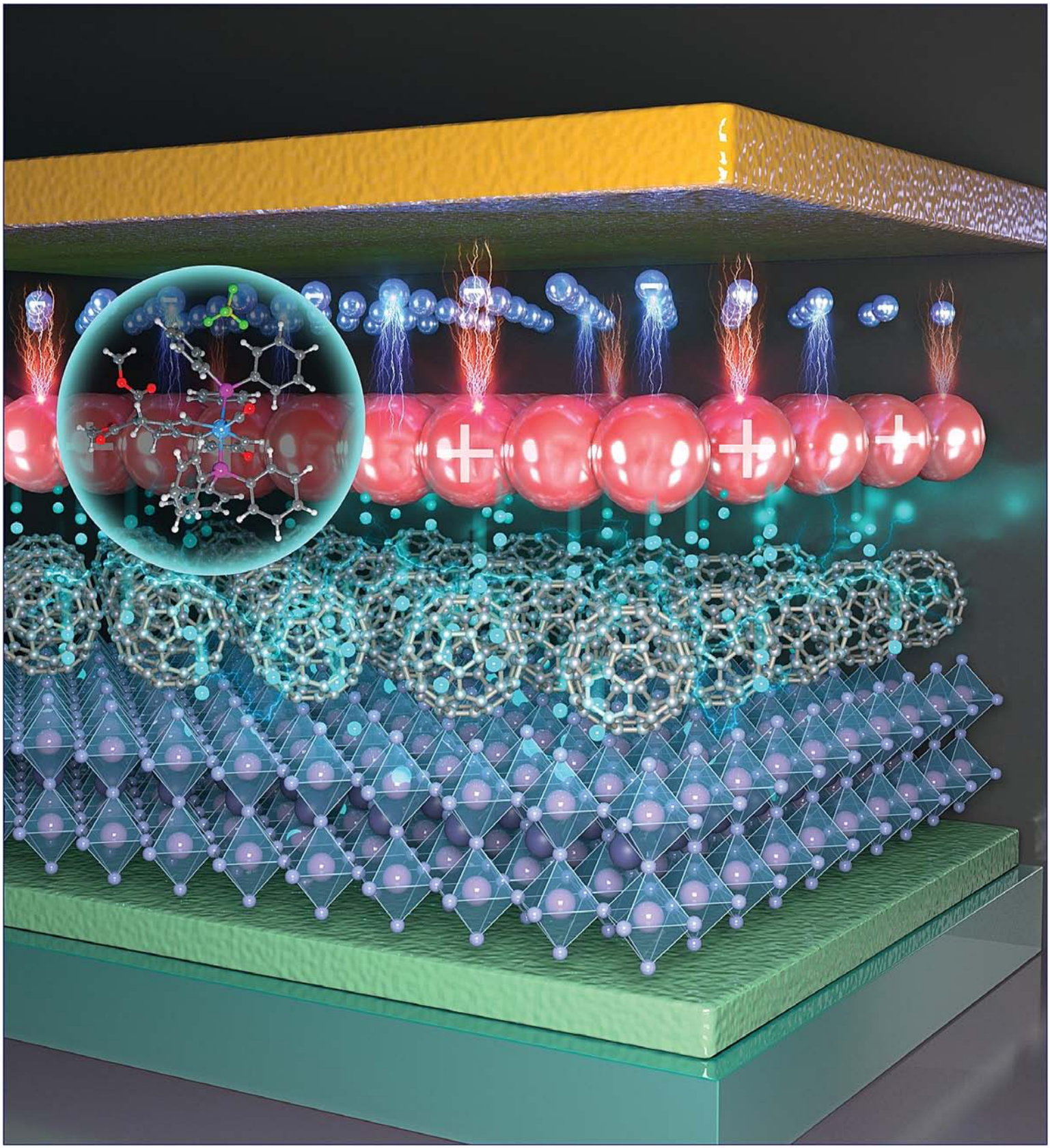

ACS Publications
Most Trusted. Most Cited. Most Read.

www.acs.org

JACS
JOURNAL OF THE AMERICAN CHEMICAL SOCIETY
pubs.acs.org/JACS
Article

Tuning an Electrode Work Function Using Organometallic Complexes in Inverted Perovskite Solar Cells

Jiantao Wang,● Jinhua Li,● Yecheng Zhou,● Chengzhuo Yu, Yuhui Hua, Yinye Yu, Ruxue Li, Xiaosong Lin, Rui Chen, Hongkai Wu, Haiping Xia,* and Hsing-Lin Wang*

Cite This: J. Am. Chem. Soc. 2021, 143, 7759−7768
Read Online
ACCESS | Metrics & More | Article Recommendations | Supporting Information

ABSTRACT: Low-work-function (WF) metals (including silver (Ag), aluminum (Al), and copper (Cu)) used as external cathodes in inverted perovskite solar cells (PSCs) encounter oxidation caused by air exposure and halogen-diffusion-induced corrosion, which threaten the long-term stability of the device. The cathode interlayer (CIL) has shown promise in reducing the metal WF and thus boosting the device power conversion efficiency (PCE). However, it remains a challenge for current CIL materials to enable high-WF metals (e.g., Au) to be used as cathodes to achieve PSCs with a superior PCE and long-term stability. Here, we use a series of synthesized (carbolong-derived) organometallic complexes as CILs to tune the electrode WF in inverted PSCs. Density functional theory calculations and surface characterizations show that the organometallic complexes that contain anions and cations are prone to form anion−cation dipoles on the metal surface, hence drastically reducing the metal's WF. Photovoltaic devices based on a Ag cathode, which was modified with these organometallic complexes, received a boosted PCE up to 21.29% and a remarkable fill factor that reached 83.52%, which are attributed to the dipole-enhanced carrier transport. The environmental stability of PSCs was further improved after employing Au as a cathode with these organometallic complexes, and the modified devices exhibited no efficiency loss after 4080 h storage measurements.

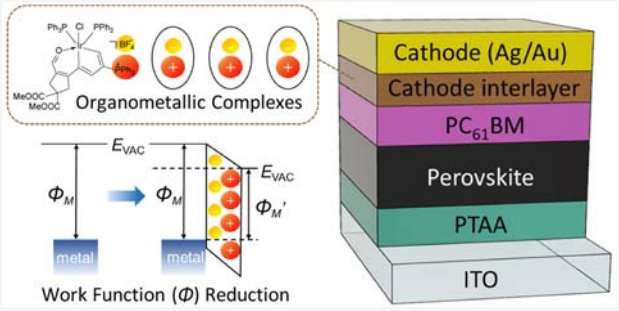

INTRODUCTION

The renewable energy community has put increasing interest on perovskite solar cells (PSCs) due to their low-cost and high-efficiency commercial prospects.[1−6] In PSCs, a perovskite layer is normally sandwiched between a transparent conductive oxide and a metal electrode, where a high-work-function (WF) metal as the anode is used to collect holes in a regular configuration or a relatively low-WF metal as the cathode to collect electrons in an inverted architecture.[7] Low-WF metals (including silver (Ag), aluminum (Al), and copper (Cu)) in inverted PSCs, however, encounter oxidation caused by air exposure and halogen-diffusion-induced corrosion, which threaten the long-term stability of photovoltaic devices.[8] An alternative approach to obtain a stable cathode is to employ a high-WF metal that is chemically stable and not easily oxidized. Additionally, to modulate the energy band alignment it is necessary to insert an ultrathin (0.5−10 nm) surface modifier between the metal and the electron transporting layer (ETL).[8] Such a cathode interlayer (CIL) is crucially important to reduce the interfacial energy barrier and protect the lower layers from the diffusion of vapor metal atoms and the penetration of ambient moisture.[9−11]

To date, CILs such as polymers, organic small-molecules, metal oxides, alkali salts, two-dimensional (2D) materials, and others have been reported to modify common electron-collecting metals.[11−19] For instance, vacuum-evaporated bathocuproine (BCP) has been widely used to obtain record efficiencies for inverted PSCs.[20,21] Besides, Chen et al. have reported solution-processed metal acetylacetonates as CILs and demonstrated their improved efficiency.[22] Furthermore, Li et al. have developed a benzotriazole (BTA) CIL that can coordinate with a Cu electrode with an anticorrosion ability, thus significantly improving the device stability.[23] However, it remains a challenge to tailor CIL materials to enable the use of high-WF metals (e.g., Au) as cathodes to achieve PSCs with a high PCE and long-term stability.

Organometallic materials whose electronic properties could be regulated by altering core metals and chelating ligands offer the potential to modulate the interfaces of photovoltaic devices. Carbolong complexes with strong metal−carbon bonds, which are formed by the chelation of a carbon chain

Received: February 25, 2021
Published: April 27, 2021

https://doi.org/10.1021/jacs.1c02118
J. Am. Chem. Soc. 2021, 143, 7759−7768

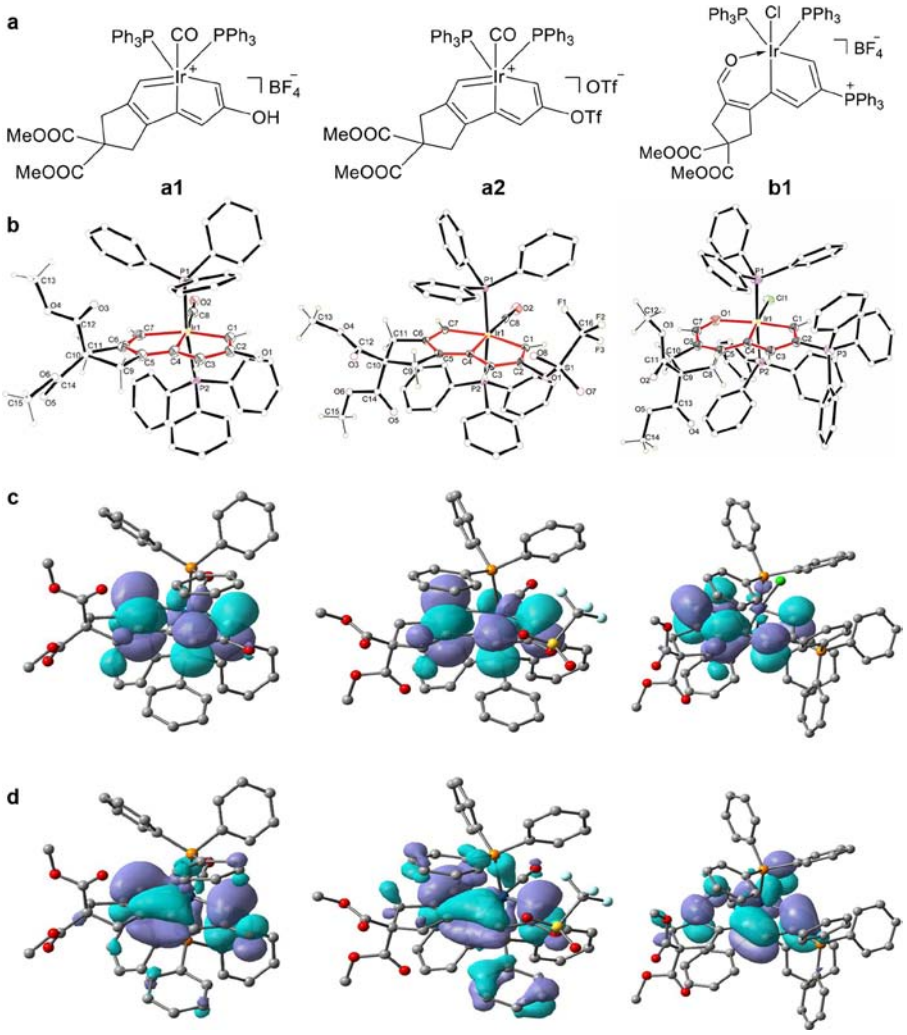

Figure 1. Molecular structures and density functional theory (DFT) calculations. (a) Molecular structures of organometallic complexes **a1**, **a2**, and **b1**. (b) X-ray molecular structures for the cations of **a1**, **a2**, and **b1** (ellipsoids are at the 50% probability level, and the hydrogen atoms of phenyl groups in PPh_3 were omitted for clarity). DFT calculations of (c) lowest unoccupied molecular orbitals (LUMOs) and (d) highest occupied molecular orbitals (HOMOs) for the cations of **a1**, **a2**, and **b1** (from left to right in each panel).

(carbolong ligand) with a transition metal fragment, are a burgeoning class of π-conjugating organometallic frameworks.[24−26] Carbolong-derived complexes have emerged as promising materials in many applications due to their excellent photophysical properties.[26,27] Recently, an osmium−carbolong complex has been successfully used as an ETL material in OSCs, which had a PCE up to 16.28%.[28]

Herein, we report a series of novel carbolong-derived frameworks that allow low- and high-WF metals to be used as cathodes for PSCs. We found the carbolong-derived complexes tend to form interfacial dipoles on the metal surface, thus decreasing the metal's WF. Inverted PSCs that employed a Ag cathode with these carbolong-derived materials achieved a champion PCE of 21.29% and a remarkable fill factor of 83.52%, which are among the highest values for inverted PSCs without passivation procedures. Mechanistic investigations showed that the carbolong-derived materials boost the device performance through dipole-enhanced charge transport. Notably, the inverted devices integrated with carbolong-derived complexes and a Au cathode had a superior environmental stability and no PCE loss after 4080 h of storage in an inert atmosphere.

RESULTS AND DISCUSSION

Design and Synthesis of Organometallic Complexes.

The molecular structures of the target carbolong-derived complexes, **a1**, **a2**, and **b1**, are presented in Figure 1a. All the molecules contain a counteranion; both **a1** and **b1** have the same anion ($[BF_4]^-$), while **a2** has a different anion ($[OTf]^-$). In contrast, the apparent positive charges are at the iridium center in all complexes except **b1**, where they are at the phosphonium group. The contrasting structures allow the structure−property−performance relationship, which is applicable to the evolution of new electrode interfacial materials for electronic and energy conversion devices, to be established.[29] The molecular synthetic procedures, nuclear magnetic resonance (NMR) characterizations, and solid-state structures by single-crystal X-ray diffraction (XRD) of **a1**, **a2**, and **b1** are shown in Figures S1−S16. The single-crystal XRD structures and density functional theory (DFT) calculations of the lowest unoccupied molecular orbitals (LUMOs) and highest occupied molecular orbitals (HOMOs) for the cations of **a1**, **a2**, and **b1** are successively exhibited on the heels of their molecular structures (Figure 1b−d, respectively). The calculated LUMOs of **a1**, **a2**, and **b1** are −5.39, −5.62, and −4.97 eV, respectively.

https://doi.org/10.1021/jacs.1c02118
J. Am. Chem. Soc. 2021, 143, 7759−7768

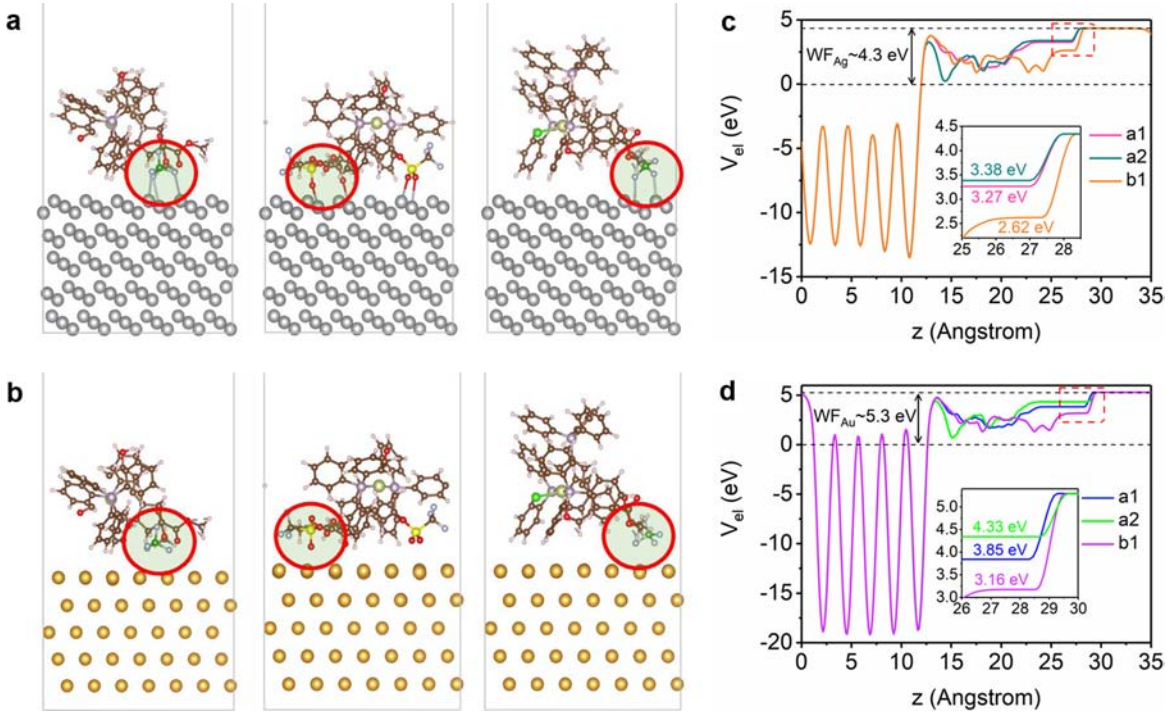

Figure 2. Density functional theory (DFT) calculations. Side view of final molecular configurations of **a1**, **a2**, and **b1** adsorbed on the (a) Ag and (b) Au surfaces. The red circles refer to the anions of organometallic complexes. Local potential curves of the final configuration models with **a1**, **a2**, and **b1** adsorbed on the (c) Ag and (d) Au surfaces.

The deep LUMOs of the cation suggest its strong electron-accepting ability, which is energetically beneficial for electron transport from the ETL to the external metal cathode.[30] The optical bandgaps that correspond to **a1**, **a2**, and **b1** are 2.17, 2.13, and 1.85 eV, respectively, which were estimated from the solution UV−vis absorption spectra (Figure S17). Differing from the solution absorption, we found a slight red-shift at the absorption onset of their as-prepared solid films (Figure S18), indicating an intermolecular interaction during film formation.[31] Such an interaction is advantageous for forming a dense and uniform film that prevents a direct contact between the metal electrode and its lower layers. Thermogravimetric analyses (TGA) of **a1**, **a2**, and **b1** show that the initial decomposition temperatures (*T*5) as measured at the point of 5% weight loss are 248.07, 233.19, and 263.52 °C, respectively (Figure S19). Excellent thermal stability is critical to circumvent the degradation caused by vapor metal atoms and allow the stable operation of solar cells. The favorable electronic and thermal properties of **a1**, **a2**, and **b1** serve the role of electrode modifiers for high performance photovoltaic devices.

Characterizations of the Metal WF Reduction. To reveal the change in the metal WF caused by the carbolong-derived molecules, we carried out density functional theory (DFT) calculations by building the adsorption models of **a1**, **a2**, and **b1** on metal surfaces. Based on the total energies of the possible molecular configurations, we found that the anion prefers to stay at the metal surface on the side of the cation (Figure S20). Based on this low-energy laydown configuration, we performed molecular dynamic simulations (Figures S21−S23) to obtain the final possible adsorption configurations of **a1**, **a2**, and **b1** on Ag (111) and Au (111) surfaces (Figure 2a and b, respectively). We compared the DFT-optimized molecular structures with the XRD structures. All the computational data regarding bond distances and bond angles (listed in Table S1) are very close to those of the experiments, suggesting that our simulations are reliable. Based on the final adsorption models, we further obtained the charge transfer (Figures S24 and S25) and the local potential between the carbolong-derived molecules and the metals, whose related values are listed in Tables S2 and S3. As shown in the local potential curves (Figure 2c), the final calculated WF of Ag is 4.3 eV, which decreased to 3.27, 3.38, and 3.62 eV after integrating with **a1**, **a2**, and **b1**, respectively. Similarly, the WF of Au is decreased from 5.3 eV to 3.85, 4.33, and 3.16 eV after integrating with **a1**, **a2**, and **b1**, respectively (Figure 2d).

Generally, the anions in **a1**, **a2**, and **b1** are prone to adsorb on the metal surface, and the cations are distributed spatially above the anions (Figure S26) where the anions and cations will form interfacial dipole moments (μ_{ID}). Due to the dipole moments that exist on the metal surface, the vacuum energy level (E_{vac}) of the electrons should be steeply shifted (Figure S27). In this case, the apparent WF of the metal will decrease.[8,32] In view of the cation−anion dipole formation, all carbolong-derived molecules are able to significantly lower the WF of Ag and Au. First-principle calculations demonstrated that the change of the WF shows very little dependence on the charge transferred from the metal surface to the molecules but instead displays a general increase with the dipole moments of the carbolong-derived molecules. However, the dipole moments of the molecules were altered due to the charge transfer among the metal surface, the cation, and the anion. The charge transfer also induces dipole moments at the cation−surface and anion−surface contacts. Therefore, the WF alteration should depend on the dipole moments of the cation−anion, cation−surface, and anion−surface pairs. Specifically, calculations show that the dipole moments of the anion−surface pair induce a slight increase of the metal WF, where the anion

https://doi.org/10.1021/jacs.1c02118
J. Am. Chem. Soc. 2021, 143, 7759−7768

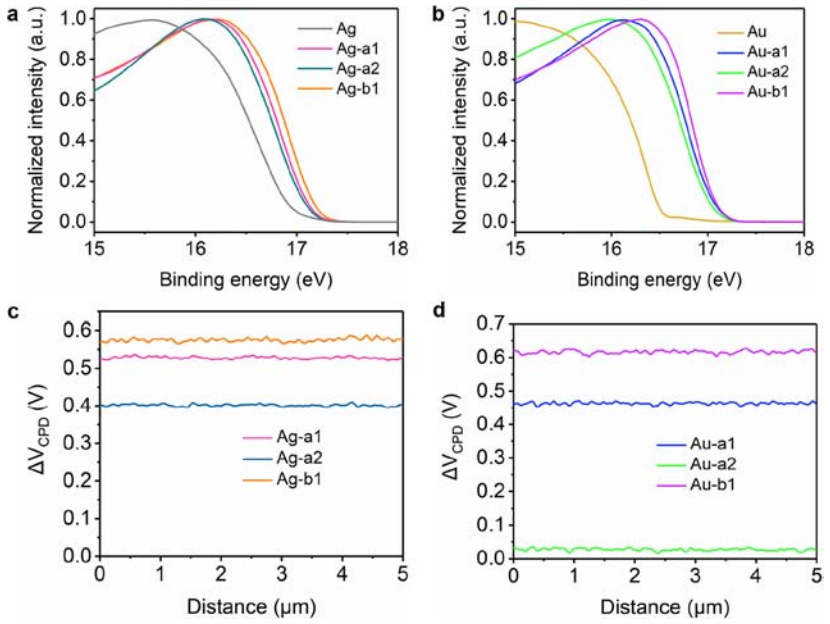

Figure 3. Surface work function characterizations. Normalized ultraviolet photoelectron spectroscopy (UPS) intensity of the (a) Ag and (b) Au surfaces with or without the coverage of **a1**, **a2**, and **b1**. Contact potential difference (ΔVCPD) before and after **a1**, **a2**, and **b1** deposition on the (c) Ag and (d) Au surfaces measured by scanning Kelvin probe microscopy (SKPM).

$[OTf]^-$ in **a2** exhibits a greater impact than that of $[BF_4]^-$ in **a1** and **b1**. Notably, the [OTf] group in the framework has negative effects on the WF decrease, probably due to the strong electron-withdrawing character, which leads to **a2** having the worst capacity for WF reduction. Even so, all the dipole moments of the cation−surface pair reinforce the WF decrease as they have the same μ_{ID} direction as the cation−anion dipole moments. The best capacity of **b1** for WF reduction is probably due to the stronger dipole moments of the cation−anion and cation−surface pairs, which originate from the lateral positive charge in the phosphonium group that is closer to the metal surface and the anion. Overall, the WF reduction is mainly derived from the molecular cation−anion dipole on the metal surface as well as the cation−surface dipole; nevertheless, the anions, especially the [OTf] group, restrain the WF decrease to some degree.

To experimentally assess the decreases of the metal WF induced by these carbolong-derived materials, we performed surface characterizations, including ultraviolet photoelectron spectroscopy (UPS) and scanning Kelvin probe microscopy (SKPM). The measured surface WF values are summarized in Table S2. For UPS performed under an ultrahigh vacuum, the WF of bare Ag (4.26 eV) was reduced to 4.09, 4.13, and 3.89 eV after coverage with **a1**, **a2**, and **b1**, respectively, and that of bare Au (4.70 eV) was reduced to 4.18, 4.21, and 4.11 eV for the **a1**, **a2**, and **b1** modifications, respectively. Panels a and b of Figure 3 show the normalized UPS intensity of the Ag and Au surface, respectively with or without the deposition of **a1**, **a2**, and **b1**. Compared comprehensively, the UPS results reveal the trend **a2** < **a1** < **b1** for the extent of the WF reduction for the Ag and Au surfaces. SKPM is a more convenient method for determining the WF of a metal.[22,33] The contact potential difference (ΔV_{CPD}) before and after the deposition of **a1**, **a2**, and **b1** can be calculated by using SKPM to measure their V_{cp} values in air (Figures S28 and S29). The line profiles of ΔV_{CPD} (Figure 3c, d) reveal that the extent of the WF reduction ($\Delta\varphi_M = -e\Delta V_{CPD}$) of Ag and Au follows the sequence **a2** < **a1** < **b1**. Both SKPM and UPS suggest the same WF reduction trend of **a2**, **a1**, and **b1**, arranged from small to large order, which agrees well with the DFT calculations. The DFT calculations and surface characterization results offer possibilities for rationally designed organometallic materials to further improve the performances of photovoltaic devices.

Applications in Inverted PSCs. Perovskite photovoltaic devices with regular (planar or mesoporous) configurations are epidemic yet commonly require high-temperature-processed TiO_2 as an electron transporting layer or doped spiro-OMeTAD as a hole transporting layer, which restricts their realistic industrializations. In contrast, a planar inverted configuration allows the use of low-temperature, solution-processed, and dopant-free organic hole or electron transporting layers that have the advantages of straightforward fabrication, negligible hysteresis, stable device efficiency, and applicability in flexible and tandem devices. To exploit the above carbolong-derived complexes as a cathode interlayer (CIL) in inverted perovskite solar cells (PSCs), we fabricated a photovoltaic device with the architecture of ITO/PTAA/perovskite/$PC_{61}BM$/CIL/cathode (Figure 4a); the cross-sectional morphology recorded with SEM is shown in Figure S30a.[34,35] One of the most popular perovskite compositions used to fabricate highly efficient and stable PSCs is $(CsPbI_3)_{0.05}[(FAPbI_3)_{0.83}(MAPbBr_3)_{0.17}]_{0.95}$. Here, we selected the perovskite composition $(CsPbI_3)_{0.05}[(FAPbI_3)_{0.90}(MAPbBr_3)_{0.10}]_{0.95}$ with an increased $FAPbI_3$ ratio and hence a narrower bandgap to achieve a higher current density, which is necessary to obtain superb device performance. The carbolong-derived complexes were used as the CIL, which was 8−10 nm as measured with AFM (Figure S30b) and was inserted between $PC_{61}BM$ and the cathode. We first conducted the numerical simulations for $J-V$ curves of this inverted PSC under a different WF cathode (Figure 4b). The parameters used for numerical simulations were listed in Table S4. The simulated $J-V$ curves indicate that the high-WF (4.3 eV) cathode will markedly increase the

https://doi.org/10.1021/jacs.1c02118
J. Am. Chem. Soc. 2021, 143, 7759−7768

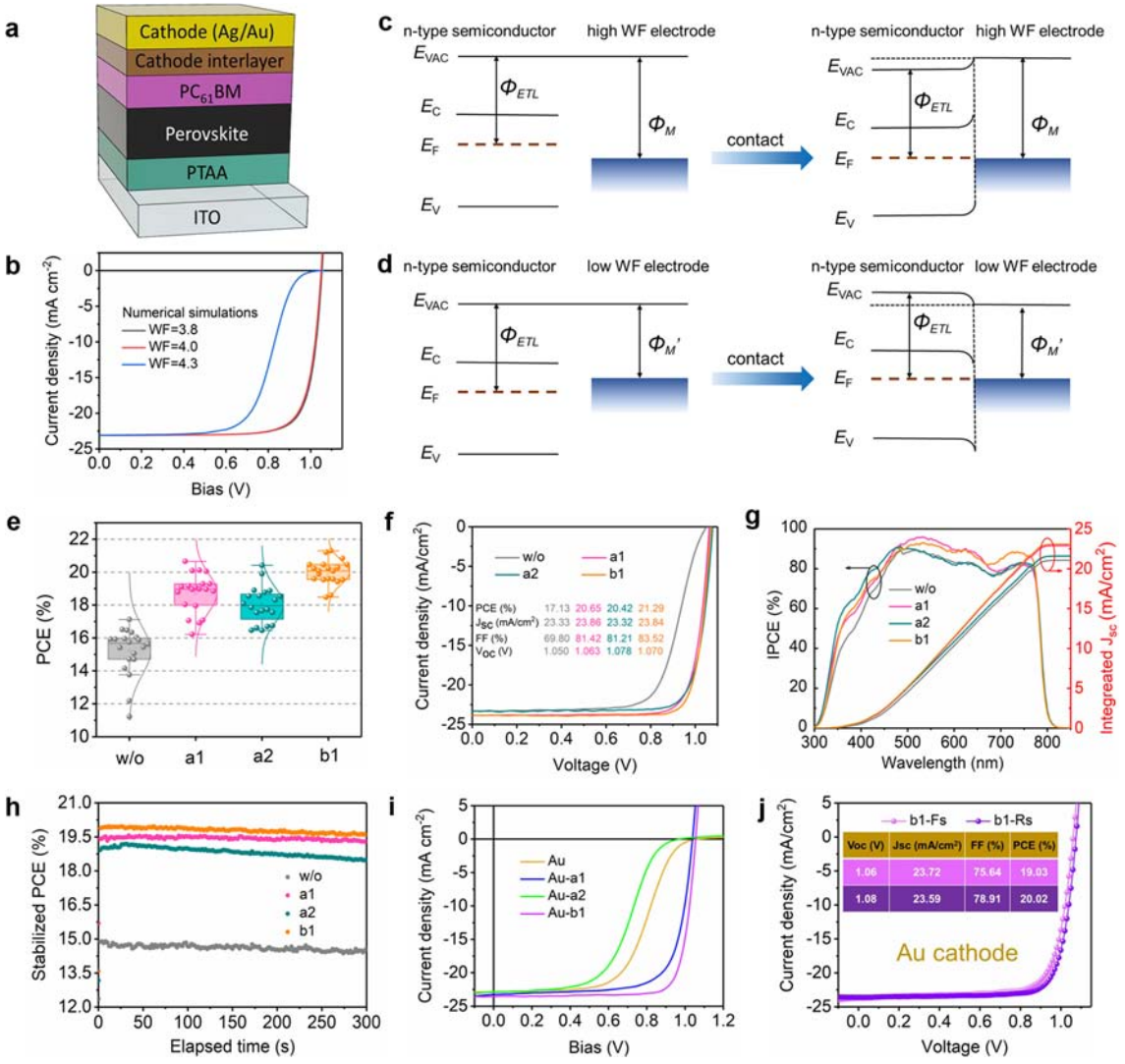

Figure 4. Device performances. (a) Device structure. (b) Numerical simulated $J-V$ curves of solar cell models with different work functions of cathodes that are 3.8, 4.0, and 4.3 eV. Illustration of band bending in the condition of (c) a high-WF and (d) a low-WF metal as the cathode. (e) PCE statistics based on 20 cells. (f) $J-V$ curves (reverse scan) of champion devices based on a Ag cathode. (g) IPCE and integrated J_{sc} of the champion devices based on a Ag cathode. (h) Stabilized PCE output under the bias of a maximum-power point. (i) $J-V$ curves of solar cells based on a Au cathode with or without the modification of carbolong-derived complexes. (j) $J-V$ curves of the champion device based on a Au cathode.

interfacial contact resistance and result in the appearance of an S-shape kink in the $J-V$ curves. On the other hand, the S-shape kink can be eliminated once the cathode WF is reduced to a sufficiently low extent (4.0 eV). However, the device PCE will hardly increase, as the modifiers reduce the cathode WF to the near-saturation level (3.8 eV). The influence of the cathode WF on the interfacial band alignment is shown in Figure 4c and d. A thick organic semiconductor ($PC_{61}BM$) will form a Schottky junction with the metal in solar cells that commonly features metallic external contacts, including Ag or Au. Before contact, the high-WF metal and the organic layer have WFs ϕ_M and ϕ_O ($\phi_M > \phi_O$), respectively. After contact, the Fermi level of the organic materials will align to the highest occupied electron energy of the metal. Simultaneously, a downward shift in the vacuum level and band bending formed in the $PC_{61}BM$ results in the formation of a Schottky barrier that hinders the electron transport. To eliminate the Schottky barrier and form an Ohmic contact for a photovoltaic device, an ultrathin interlayer should be inserted to separate both layers. This ultrathin interlayer can reduce the WF of a metal and turn it into a low-WF cathode. As depicted in Figure 4d, using the CIL-modified metals as a low-WF cathode will lead to an upshift of the vacuum level, thus resulting in a high collection efficiency of electrons.

The statistical PCEs of the devices based on a Ag cathode are shown in Figure 4e. Their photovoltaic characteristics, such as the open-circuit voltage (V_{oc}), the short-circuit current density (J_{sc}), and the fill factor (FF), are listed in Table S5. The devices exhibit improved average V_{oc}, J_{sc}, and FF values after the incorporation of **a1**, **a2**, and **b1** CILs; thus, the average PCE was boosted from 15.21 ± 1.42% of the pristine devices to 18.73 ± 1.15%, 18.01 ± 1.75%, and 19.99 ± 0.71%, respectively. The $J-V$ curves and derived parameters of the champion devices (Figure S31) show suppressed hysteresis after employing **a1**, **a2**, and **b1**. The characteristics of these curves (Figure 4f) are in accordance with the simulated results in Figure 4b, signifying the decreased WF of the cathode and the reduced interfacial energy barrier acquired by the modification of CILs. It is noted that the **b1**-modified device harvests a 21.29% champion PCE and a remarkable FF of

https://doi.org/10.1021/jacs.1c02118
J. Am. Chem. Soc. 2021, 143, 7759−7768

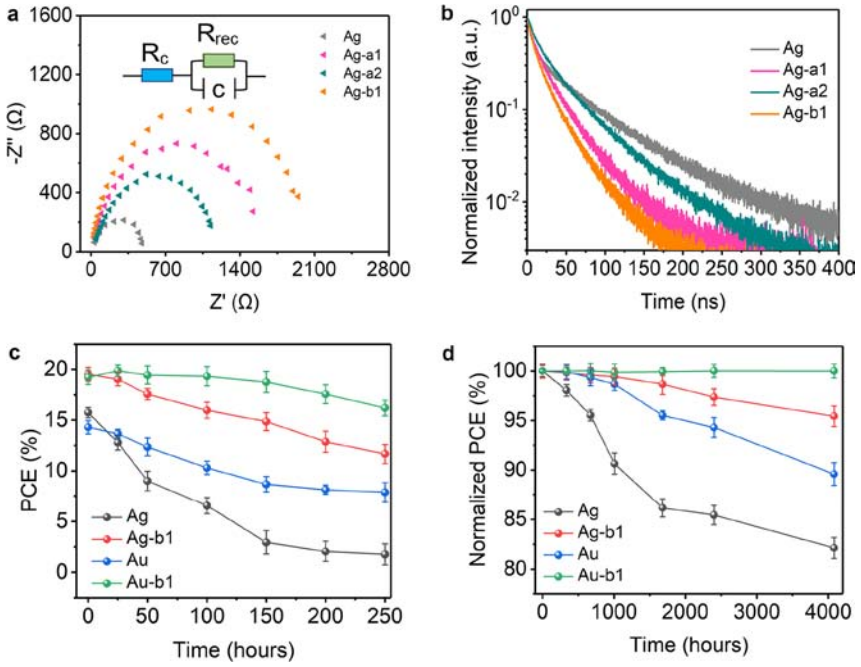

Figure 5. Device characterizations. (a) Electrochemical impedance spectrum (EIs) and (b) time-resolved photoluminescence (TRPL) of inverted perovskite solar cells. (c) Environmental and (d) long-term storage stability measurements of pristine and **b1**-modified devices based on Ag and Au cathodes without encapsulation.

83.52%, which are among the highest values based on this device structure without passivation procedures. The integrated J_{sc} values derived from the incident photon to current efficiency (IPCE) are 21.07, 22.90, 21.60, and 23.07 mA cm^{-2} for device without CIL and with **a1**, **a2**, and **b1**, respectively (Figure 4g), which are very consistent with the J_{sc} values measured from the $J-V$ curves. We obtained the steady-state PCE output as a function of time by multiplying the current density with the photovoltage at the maximum-power point (MPP). The MPP output is 14.7% for the pristine device and 19.4%, 19.2%, and 19.9% for **a1**-, **a2**-, and **b1**-modified devices, giving an accurate confirmation of the device performances (Figure 4h). Specifically, the carbolong-derived complexes **a1**, **a2**, and **b1** as CILs show a remarkable compatibility toward the high-WF cathode in PSCs. We ulteriorly replaced the reactive Ag with the high-WF Au, and their performance parameters are listed in Table S6. The average PCE was boosted from 12.95 ± 0.94% of the pristine devices to 17.44 ± 1.72%, and 19.31 ± 0.73% after the integration of **a1** and **b1**, respectively. However, the introduction of **a2** only achieved an average PCE of 10.17 ± 1.04%, which is lower than that of the pristine device. Their $J-V$ curves (Figure 4i) reflect the formation of an Ohmic contact at the $PC_{61}BM$−cathode interface after the modification of **a1** and **b1** due to the drastic reduction of the energy barrier, as illustrated in panels c and d, respectively of Figure 4. S-shaped kinks in the $J-V$ curves of devices with and without **a2** reveal the existence of a large interfacial contact resistance.[36] Moreover, there is a WF increase and thus a larger interfacial contact resistance after the introduction of **a2** compared to the pristine device. The larger contact resistance of the **a2**-modified device is presumably due to the strong interaction of [OTf] groups, which can increase the metal WF upon contact with higher-temperature thermally evaporated Au atoms. The champion device based on a Au cathode achieved a PCE as high as 20.02% under the incorporation of **b1** (Figure 4j). It exhibits a higher V_{oc} value but lower FF and J_{sc} values compared to those of the pristine device, likely owing to the decreased contact resistance of the Ag cathode.

We assumed that the boosted photovoltaic parameters (V_{oc}, J_{sc}, FF, and PCE) resulted from the lower-energy-barrier transport of the interfacial carriers. To study the transport dynamics of the interfacial carriers of Ag cathode-based devices, we performed electrochemical impedance spectroscopy (EIs) and time-resolved photoluminescence (TRPL) measurements.[37] The Nyquist plots of EIs based on devices with or without **a1**, **a2**, and **b1** are displayed in Figure 5a. The interfacial resistances mainly contain a charge transport resistance (R_C) and a charge recombination resistance (R_{REC}), as shown by the equivalent circuit in the inset.[38] The Ag cathode device without a CIL displays a maximum R_C and a minimum R_{REC}. After **a2**, **a1**, and **b1** modification, the devices present decreasing R_C values (**a2** > **a1** > **b1**) and increasing R_{REC} values (**a2** < **a1** < **b1**), signifying the facilitated electron transport from ETL to the cathode due to the reduced interfacial energy barrier. The TRPL decay spectra of the four complete devices are presented in Figure 5b and fitted with a biexponential decay that consists of a fast component (τ_1) and a slow component (τ_2),[39] and the derived data are listed in Table S7. The lifetimes of both the fast and slow components follow the sequence **b1** < **a1** < **a2** < without, where the lifetimes of τ_1 and τ_2 for **a2** are larger than those of **a1** and **b1**. This contributes to the lower PCE that was obtained when employing **a2** due to the faster electron transport for the shorter-lifetime (**a1** and **b1**) devices. Decay lifetime averages τ_{av} ($\tau_{av} = A_1\tau_1 + A_2\tau_2$) of 30.459, 46.094, and 25.103 ns for **a1**-, **a2**-, and **b1**-modified devices are faster than that of the pristine device at 67.042 ns, indicating a facilitated electron transport that is in perfect agreement with the carrier mobility order (**b1** > **a1** > **a2** > pristine device) derived from the space-charge-limited current (SCLC) curves (Figure S32).

In terms of the high efficiency of **b1**-based devices, we measured the ambient and storage stabilities of unencapsulated

https://doi.org/10.1021/jacs.1c02118
J. Am. Chem. Soc. 2021, 143, 7759−7768

inverted PSCs based on Ag and Au cathodes with or without the **b1** modification. As depicted in Figure 5c, **b1** embodied devices present higher PCEs within 250 h in the air condition (>50% humidity) than the devices without CILs, and the environmentally stable Au-based device exhibits a much slower PCE decrease. The results disclosed that the Au-based devices with a **b1** complex as the CIL prolong the environmental lifespan of inverted PSCs. We also measured the long-term stability of these devices ,which were stored in glovebox with an inert atmosphere (Figure 5d). After inserting **b1**, the modified devices exhibited enhanced normalized PCEs with a function of the storage time compared to those of the pristine devices. Peculiarly, the PCE of the Au-based devices with **b1** remained unchanged after 4080 h, while others presented continuous attenuation. We further performed operational stability measurements of the unencapsulated devices based on a Au cathode with or without the incorporation of **b1** (Figure S33). The Au-based device with **b1** showed a nearly unchanged PCE (~20%) under 250 h of MPP tracking at continuous light irradiation with a white LED lamp (100 mW cm^{-2}) in a N_2-filled glovebox, while the initial PCE (~12%) of the CIL-free device decreased to 80% of its value (~9.6% PCE) after 110 h. Therefore, the high-WF metal with carbolong-derived complexes for a stable cathode is significant to achieve a superior stability for inverted PSCs.

CONCLUSION

In summary, we have designed and synthesized a series of the organometallic complexes as CILs to achieve a low-WF cathode for inverted PSCs. The dipole moments formed by anions and cations of the tailored complexes change the work function of both the reactive metal Ag and the environmentally stable Au to a sufficiently low extent. Benefiting from the electrode interfacial modulation, the low-WF cathode for inverted PSCs boosts the PCE up to 21.2% for Ag-based devices and 20.02% for Au-based devices. Specifically, we further achieved an improved environmental stability and long-term (4080 h) identical PCE values by employing a Au cathode. The solution-processed carbolong-derived organometallic complexes would provide a cost-efficient way to boost the photovoltaic performance for flexible and tandem PSCs toward large-scale fabrication. Organometallic materials have provided new opportunities for the interfacial modulation of metal−semiconductor contacts in PSCs and would also have potential applications in other electronic devices, such as organic solar cells, light emitting devices, and thin-film transistors.

EXPERIMENTAL SECTION

Materials. All the reagents were used as received from commercial sources without further purification. Lead(II) dibromide ($PbBr_2$), methylammonium bromide (MABr), formamidinium iodide (FAI), and PTAA (M_n = 5,000−15,000) were purchased from Xi'an Polymer Light Technology Corp (China). Lead(II) diiodide (PbI_2, 99.999%) and indium tin oxide (ITO, sheet resistance < 10 Ω) glass were purchased from Advanced Election Technology Co., Ltd. (China). Anhydrous liquid reagents, including *N*,*N*-dimethylformamide (DMF), dimethyl sulfoxide (DMSO), chlorobenzene (CB), and ethanol, were purchased from J&K and used as received. Diethyl ether was distilled from sodium/benzophenone and dichloromethane was distilled from calcium hydride under N_2 prior to use. Phenyl-C_{61}-butyric acid methyl ester ($PC_{61}BM$, 99.5%) was purchased from Shanghai Da Ran Chemicals. Silver (Ag, 99.99%) and gold (Au, 99.99%) were obtained from commercial sources.

Synthesis and Structural Characterizations of Carbolong-Derived Complexes. All syntheses were performed under a N_2 atmosphere using standard Schlenk techniques unless otherwise stated. Compounds **1** and **2** were synthesized according to previously published procedures.[40,41] Column chromatography was performed on neutral alumina (200−300 mesh) in air. NMR spectroscopic experiments were performed on a Bruker AVIII-400 (^{1}H, 400.1 MHz; ^{13}C, 100.6 MHz; ^{31}P, 162.0 MHz) spectrometer, a Bruker AVIII-500 (^{1}H, 500.2MHz; ^{13}C, 125.8 MHz; ^{31}P, 202.5 MHz) spectrometer, or a Bruker Ascend III 600 (^{1}H, 600.1 MHz; ^{13}C, 150.9 MHz; ^{31}P, 242.9 MHz) spectrometer at room temperature. The ^{1}H and ^{13}C NMR chemical shifts (δ) are reported relative to tetramethylsilane, and the ^{31}P NMR chemical shifts are relative to 85% H_3PO_4. The absolute values of the coupling constants are given in hertz (Hz). Multiplicities are abbreviated as singlet (s), doublet (d), triplet (t), multiplet (m), and broad (br). HRMS experiments were performed on a Bruker En Apex Ultra 7.0T FT-MS instrument. Absorption spectra were recorded on an Agilent Cary 5000 UV−vis spectrophotometer.

X-ray Crystallographic Analysis. The crystals suitable for X-ray diffraction were grown from a CH_2Cl_2 solution layered with ethyl ether for complexes **a1**, **a2**, **3**, and **b1**. Single-crystal X-ray diffraction data were collected on an Xcalibur Sapphire3 Gemini ultra detector with graphite-monochromated Cu Kα radiation (λ = 1.54184 Å) for **a1**. Data for **a2** were collected on a Bruker PHOTO 100 area detector with graphite-monochromated Mo Kα radiation (λ = 0.71073 Å). Data for **3** were collected on a Bruker CMOS area detector with mirror-monochromated Mo Kα radiation (λ = 0.71073 Å). Data for **b1** were collected on a Sapphire3 CCD plate detector with graphite-monochromated Mo Kα radiation (λ = 0.71073 Å). All the data were corrected for absorption effects using the multiscan technique. Using Olex2,[42] the structures of **a1**, **a2**, **3**, and **b1** were solved with the XT[43] structure solution program using intrinsic phasing; all the structures were refined with the ShelXL[44] refinement package using least-squares minimization. All the non-hydrogen atoms were refined anisotropically unless otherwise stated. The hydrogen atoms were placed at their idealized positions and refined using a riding model unless otherwise stated. The solvents CH_2Cl_2 and H_2O and the phenyl groups on PPh_3 were disordered and refined using restraints.

Fabrication of Inverted PSCs. MABr (0.14 M), $PbBr_2$ (0.14 M), FAI (1.26 M), and PbI_2 (1.36 M) were weighed in a brown vial in the glovebox. To the vial was added 1 mL of the mixed solvent DMF/DMSO (4/1, v/v), and the solution was stirred at 65 °C for an hour. Then, 40 μL of CsI (2M) in DMSO was added, and the mixed precursor was stirred at 65 °C for 15 min. Fresh solution was used every time. The PTAA stock solution was prepared by weighing 6 mg of PTAA into 1 mL of CB without dopant. We prepared the $PC_{61}BM$ solution by dissolving 20 mg of $PC_{61}BM$ into 1 mL of CB and stirring the mixture at 70 °C for 2 h. Patterned ITO glasses were cleaned by sonication using detergent, acetone, and isopropanol for 20 min each. The nitrogen-dried ITO glasses were further treated by air plasma for 4 min and then transferred into the glovebox for further spin-coating processes. First, 3 mg mL^{-1} PTAA was spin-coated at 6000 rpm for 30 s, followed heating at 100 °C for 10 min. The perovskite precursor was deposited in two-step spin-coating program as follows: 1000 rpm for 10 s and then 5000 rpm for 30 s, with a treatment with 250 μL of CB at 8 s before the end of the high-speed step. The substrate was immediately postannealed at 100 °C for 20 min. Then, 20 mg mL^{-1} $PC_{61}BM$ was spin-coated on the perovskite layer at 1000 rpm for 45 s. An ethanol solution with or without cathode modifiers was spin-coated at 5000 rpm for 60 s. Finally, 100 nm Ag was deposited by the thermal evaporator. The active device area of 4 mm^2 is defined by the overlap between ITO and the metal electrode.

Film Characterizations and Device Measurements. A UV−vis spectrophotometer (Agilent Cary 5000) was used to measure the absorbance of the solution and films. The surface topography and surface potential were simultaneously detected by atomic force microscopy (AFM, Asylum Research MFP-3D-Stand Alone). Ultraviolet photoelectron spectroscopy (UPS) was performed with a non-monochromated He Iα photon source ($h\nu$ = 21.22 eV) to detect the Fermi level and the HOMO of carbolong complexes deposited on the

https://doi.org/10.1021/jacs.1c02118
J. Am. Chem. Soc. 2021, 143, 7759−7768

evaporated metals. Device current density−voltage ($J-V$) curves were collected using a source meter (Keysight B2901A) and a solar simulator (Enlitech SS-F5-3A). The device $J-V$ curves were measured at 10 mV intervals and a 10 ms delay time for the forward and reverse scans under AM 1.5 G at a light intensity illumination of 100 mW cm^{-2}. The incident photon to current efficiency (IPCE) spectra were recorded with a quantum efficiency measurement system (Enlitech QER-3011) in which the light intensity at every wavelength was calibrated with a Si detector before measurement. The maximum-power point (MPP) output was measured by testing the steady-state current density at the maximum-power-point voltage. Electrochemical impedance spectroscopy (EIs) was performed in the frequency range from 200 Hz to 2 MHz by an electrochemical workstation (Princeton Applied Research, P4000+) in dark conditions at an open-circuit voltage. Time-resolved photoluminescence (TRPL) spectra were recorded with a fluorescence spectrometer (Fluo Time 300). The electron-only devices with an architecture of ITO/SnO_2/perovskite/$PC_{61}BM$/cathode interlayer/Ag were measured under dark conditions with a scan range from 0 to 5 V. All the above device measurements were performed in a nitrogen-filled glovebox.

■ ASSOCIATED CONTENT

Supporting Information

The Supporting Information is available free of charge at https://pubs.acs.org/doi/10.1021/jacs.1c02118.

Experimental details, supplementary notes, figures, and tables (PDF)

Accession Codes

CCDC 2056352−2056353, 2056357, and 2056359 contain the supplementary crystallographic data for this paper. These data can be obtained free of charge via www.ccdc.cam.ac.uk/data_request/cif, or by emailing data_request@ccdc.cam.ac.uk, or by contacting The Cambridge Crystallographic Data Centre, 12 Union Road, Cambridge CB2 1EZ, UK; fax: +44 1223 336033.

■ AUTHOR INFORMATION

Corresponding Authors

Hsing-Lin Wang − *Department of Materials Science and Engineering and Guangdong Provincial Key Laboratory of Energy Materials for Electric Power, Southern University of Science and Technology, Shenzhen 518055, China;* orcid.org/0000-0002-6379-0519; Email: wangxl3@sustech.edu.cn

Haiping Xia − *Department of Chemistry, Shenzhen Grubbs Institute, Southern University of Science and Technology, Shenzhen 518055, China*; Email: xiahp@sustech.edu.cn

Authors

Jiantao Wang − *Department of Materials Science and Engineering, Southern University of Science and Technology, Shenzhen 518055, China; Department of Chemistry, Hong Kong University of Science and Technology, Hong Kong, China;* orcid.org/0000-0002-1929-3339

Jinhua Li − *Department of Chemistry, Shenzhen Grubbs Institute, Southern University of Science and Technology, Shenzhen 518055, China*

Yecheng Zhou − *School of Materials Science and Engineering, Sun Yat-sen University, Guangzhou 510275, China;* orcid.org/0000-0001-8222-7193

Chengzhuo Yu − *Department of Materials Science and Engineering, Southern University of Science and Technology, Shenzhen 518055, China*

Yuhui Hua − *Department of Chemistry, Shenzhen Grubbs Institute, Southern University of Science and Technology, Shenzhen 518055, China*

Yinye Yu − *School of Materials Science and Engineering, Sun Yat-sen University, Guangzhou 510275, China*

Ruxue Li − *Department of Electrical and Electronic Engineering, Southern University of Science and Technology, Shenzhen 518055, China*

Xiaosong Lin − *Department of Materials Science and Engineering, Southern University of Science and Technology, Shenzhen 518055, China*

Rui Chen − *Department of Electrical and Electronic Engineering, Southern University of Science and Technology, Shenzhen 518055, China;* orcid.org/0000-0002-0445-7847

Hongkai Wu − *Department of Chemistry, Hong Kong University of Science and Technology, Hong Kong, China;* orcid.org/0000-0002-7766-7888

Complete contact information is available at: https://pubs.acs.org/10.1021/jacs.1c02118

Author Contributions

●These authors contributed equally.

Notes

The authors declare no competing financial interest.

■ ACKNOWLEDGMENTS

The authors acknowledge the funding supports from the Key-Area Research and Development Program of Guangdong Province (2019B010941001), the Shenzhen Basic Research Fund (CYJ20170817110652558), the Shenzhen Science and Technology Basic Research Program (JCYJ20170817105201098), the National Natural Science Foundation of China (nos. U1705254, 21931002, ZDSYS20180208184346531, and 2018B030322001), and the Guangdong Provincial Key Laboratory of Energy Materials for Electric Power (2018B030322001).

■ REFERENCES

(1) Jeong, M.; Choi, I. W.; Go, E. M.; Cho, Y.; Kim, M.; Lee, B.; Jeong, S.; Jo, Y.; Choi, H. W.; Lee, J.; Bae, J. H.; Kwak, S. K.; Kim, D. S.; Yang, C. Stable perovskite solar cells with efficiency exceeding 24.8% and 0.3-V voltage loss. *Science* **2020**, *369* (6511), 1615−1620.

(2) Zhang, J.; Zhang, W.; Cheng, H. M.; Silva, S. R. P. Critical review of recent progress of flexible perovskite solar cells. *Mater. Today* **2020**, *39*, 66−88.

(3) Chang, X.; Fang, J.; Fan, Y.; Luo, T.; Su, H.; Zhang, Y.; Lu, J.; Tsetseris, L.; Anthopoulos, T. D.; Liu, S. F.; Zhao, K. Printable CsPbI3 Perovskite Solar Cells with PCE of 19% via an Additive Strategy. *Adv. Mater.* **2020**, *32* (40), 2001243.

(4) Park, N. G.; Zhu, K. Scalable fabrication and coating methods for perovskite solar cells and solar modules. *Nat. Rev. Mater.* **2020**, *5* (5), 333−350.

(5) Li, H.; Zhang, W. Perovskite Tandem Solar Cells: From Fundamentals to Commercial Deployment. *Chem. Rev.* **2020**, *120* (18), 9835−9950.

(6) Hou, Y.; Aydin, E.; De Bastiani, M.; Xiao, C.; Isikgor, F. H.; Xue, D. J.; Chen, B.; Chen, H.; Bahrami, B.; Chowdhury, A. H.; Johnston, A.; Baek, S. W.; Huang, Z.; Wei, M.; Dong, Y.; Troughton, J.; Jalmood, R.; Mirabelli, A. J.; Allen, T. G.; Van Kerschaver, E.; Saidaminov, M. I.; Baran, D.; Qiao, Q.; Zhu, K.; De Wolf, S.; Sargent, E. H. Efficient tandem solar cells with solution-processed perovskite on textured crystalline silicon. *Science* **2020**, *367* (6482), 1135−1140.

(7) Bai, S.; Da, P.; Li, C.; Wang, Z.; Yuan, Z.; Fu, F.; Kawecki, M.; Liu, X.; Sakai, N.; Wang, J. T.; Huettner, S.; Buecheler, S.; Fahlman, M.; Gao, F.; Snaith, H. J. Planar perovskite solar cells with long-term stability using ionic liquid additives. *Nature* **2019**, *571* (7764), 245−250.
(8) Chen, Q.; Wang, C.; Li, Y.; Chen, L. Interfacial Dipole in Organic and Perovskite Solar Cells. *J. Am. Chem. Soc.* **2020**, *142* (43), 18281−18292.
(9) Yao, J.; Qiu, B. B.; Zhang, Z. G.; Xue, L. W.; Wang, R.; Zhang, C. F.; Chen, S. S.; Zhou, Q. J.; Sun, C. K.; Yang, C.; Xiao, M.; Meng, L.; Li, Y. F. Cathode engineering with perylene-diimide interlayer enabling over 17% efficiency single-junction organic solar cells. *Nat. Commun.* **2020**, *11* (1), 2726.
(10) Zhu, Z. L.; Chueh, C. C.; Lin, F.; Jen, A. K. Y. Enhanced Ambient Stability of Efficient Perovskite Solar Cells by Employing a Modified Fullerene Cathode Interlayer. *Adv. Sci.* **2016**, *3* (9), 1600027.
(11) Chen, T.; Shi, T. F.; Li, X. H.; Zheng, J. Q.; Fan, W. S.; Ni, B.; Wang, Y. Q.; Dai, J. M.; Xiao, Z. G. Efficient Perovskite Solar Cells with Titanium Cathode Interlayer. *Sol. RRL* **2018**, *2* (11), 1800167.
(12) Zhou, Y.; Fuentes-Hernandez, C.; Shim, J.; Meyer, J.; Giordano, A. J.; Li, H.; Winget, P.; Papadopoulos, T.; Cheun, H.; Kim, J.; Fenoll, M.; Dindar, A.; Haske, W.; Najafabadi, E.; Khan, T. M.; Sojoudi, H.; Barlow, S.; Graham, S.; Bredas, J. L.; Marder, S. R.; Kahn, A.; Kippelen, B. A universal method to produce low-work function electrodes for organic electronics. *Science* **2012**, *336* (6079), 327−32.
(13) Xiong, S. B.; Yuan, M.; Yang, J. M.; Song, J. N.; Guo, X. W.; Li, X.; Li, B.; Liu, X. J.; Duan, C. G.; Liu, F.; Fahlman, M.; Bao, Q. Y. Engineering of the Back Contact between PCBM and Metal Electrode for Planar Perovskite Solar Cells with Enhanced Efficiency and Stability. *Adv. Opt. Mater.* **2019**, *7* (19), 1900542.
(14) Hu, Z.; Miao, J. S.; Li, T. T.; Liu, M.; Murtaza, I.; Meng, H. Reduced interface losses in inverted perovskite solar cells by using a simple dual-functional phenanthroline derivative. *Nano Energy* **2018**, *43*, 72−80.
(15) Wu, J. L.; Huang, W. K.; Chang, Y. C.; Tsai, B. C.; Hsiao, Y. C.; Chang, C. Y.; Chen, C. T.; Chen, C. T. Simple mono-halogenated perylene diimides as non-fullerene electron transporting materials in inverted perovskite solar cells with ZnO nanoparticle cathode buffer layers. *J. Mater. Chem. A* **2017**, *5* (25), 13229−13229.
(16) Milošević, I. R.; Vasić, B.; Matković, A.; Vujin, J.; Ašbić, S.; Kratzer, M.; Griesser, T.; Teichert, C.; Gajić, R. Single-step fabrication and work function engineering of Langmuir-Blodgett assembled few-layer graphene films with Li and Au salts. *Sci. Rep.* **2020**, *10* (1), 8476.
(17) Agresti, A.; Pazniak, A.; Pescetelli, S.; Di Vito, A.; Rossi, D.; Pecchia, A.; Auf der Maur, M.; Liedl, A.; Larciprete, R.; Kuznetsov, D. V.; Saranin, D.; Di Carlo, A. Titanium-carbide MXenes for work function and interface engineering in perovskite solar cells. *Nat. Mater.* **2019**, *18* (11), 1228−1234.
(18) Rajagopal, A.; Yao, K.; Jen, A. K. Y. Toward Perovskite Solar Cell Commercialization: A Perspective and Research Roadmap Based on Interfacial Engineering. *Adv. Mater.* **2018**, *30* (32), 1800455.
(19) Wu, S.; Li, Z.; Li, M. Q.; Diao, Y.; Lin, F.; Liu, T.; Zhang, J.; Tieu, P.; Gao, W.; Qi, F.; Pan, X.; Xu, Z.; Zhu, Z.; Jen, A. K. 2D metal-organic framework for stable perovskite solar cells with minimized lead leakage. *Nat. Nanotechnol.* **2020**, *15* (11), 934−940.
(20) Jeng, J. Y.; Chiang, Y. F.; Lee, M. H.; Peng, S. R.; Guo, T. F.; Chen, P.; Wen, T. C. CH3NH3PbI3 perovskite/fullerene planar-heterojunction hybrid solar cells. *Adv. Mater.* **2013**, *25* (27), 3727−3732.
(21) Li, F.; Deng, X.; Qi, F.; Li, Z.; Liu, D.; Shen, D.; Qin, M.; Wu, S.; Lin, F.; Jang, S. H.; Zhang, J.; Lu, X.; Lei, D.; Lee, C. S.; Zhu, Z.; Jen, A. K. Regulating Surface Termination for Efficient Inverted Perovskite Solar Cells with Greater Than 23% Efficiency. *J. Am. Chem. Soc.* **2020**, *142* (47), 20134−20142.
(22) Chen, W.; Xu, L.; Feng, X.; Jie, J.; He, Z. Metal Acetylacetonate Series in Interface Engineering for Full Low-Temperature-Processed, High-Performance, and Stable Planar Perovskite Solar Cells with Conversion Efficiency over 16% on 1 cm(2) Scale. *Adv. Mater.* **2017**, *29* (16), 1603923.
(23) Li, X.; Fu, S.; Zhang, W.; Ke, S.; Song, W.; Fang, J. Chemical anti-corrosion strategy for stable inverted perovskite solar cells. *Sci. Adv.* **2020**, *6* (51), eabd1580.
(24) Zhuo, Q.; Zhang, H.; Hua, Y.; Kang, H.; Zhou, X.; Lin, X.; Chen, Z.; Lin, J.; Zhuo, K.; Xia, H. Constraint of a ruthenium-carbon triple bond to a five-membered ring. *Sci. Adv.* **2018**, *4* (6), eaat0336.
(25) Zhuo, Q. D.; Zhang, H.; Ding, L. T.; Lin, J. F.; Zhou, X. X.; Hua, Y. H.; Zhu, J.; Xia, H. P. Rhodapentalenes: Pincer Complexes with Internal Aromaticity. *iScience* **2019**, *19*, 1214−1224.
(26) Zhu, C.; Xia, H. Carbolong Chemistry: A Story of Carbon Chain Ligands and Transition Metals. *Acc. Chem. Res.* **2018**, *51* (7), 1691−1700.
(27) Zhou, X.; Pang, X.; Nie, L.; Zhu, C.; Zhuo, K.; Zhuo, Q.; Chen, Z.; Liu, G.; Zhang, H.; Lin, Z.; Xia, H. Successive modification of polydentate complexes gives access to planar carbon- and nitrogen-based ligands. *Nat. Commun.* **2019**, *10* (1), 1488.
(28) Chen, S. Y.; Liu, L. Z.; Gao, X.; Hua, Y. H.; Peng, L. X.; Zhang, Y.; Yang, L. L.; Tan, Y. Z.; He, F.; Xia, H. P. Addition of alkynes and osmium carbynes towards functionalized dπ-pπ conjugated systems. *Nat. Commun.* **2020**, *11* (1), 4651.
(29) Yen, H. J.; Tsai, H.; Zhou, M.; Holby, E. F.; Choudhury, S.; Chen, A.; Adamska, L.; Tretiak, S.; Sanchez, T.; Iyer, S.; Zhang, H.; Zhu, L.; Lin, H.; Dai, L.; Wu, G.; Wang, H. L. Structurally Defined 3D Nanographene Assemblies via Bottom-Up Chemical Synthesis for Highly Efficient Lithium Storage. *Adv. Mater.* **2016**, *28* (46), 10250−10256.
(30) Shimizu, T. K.; Jung, J.; Otani, T.; Han, Y. K.; Kawai, M.; Kim, Y. Two-Dimensional Superstructure Formation of Fluorinated Fullerene on Au(111): A Scanning Tunneling Microscopy Study. *ACS Nano* **2012**, *6* (3), 2679−2685.
(31) Wang, Y.; Chen, W.; Wang, L.; Tu, B.; Chen, T.; Liu, B.; Yang, K.; Koh, C. W.; Zhang, X.; Sun, H.; Chen, G.; Feng, X.; Woo, H. Y.; Djurisic, A. B.; He, Z.; Guo, X. Dopant-Free Small-Molecule Hole-Transporting Material for Inverted Perovskite Solar Cells with Efficiency Exceeding 21%. *Adv. Mater.* **2019**, *31* (35), 1902781.
(32) Zhang, Q.; Wang, W. T.; Chi, C. Y.; Wachter, T.; Chen, J. W.; Tsai, C. Y.; Huang, Y. C.; Zharnikov, M.; Tai, Y.; Liaw, D. J. Toward a universal polymeric material for electrode buffer layers in organic and perovskite solar cells and organic light-emitting diodes. *Energy Environ. Sci.* **2018**, *11* (3), 682−691.
(33) Melitz, W.; Shen, J.; Kummel, A. C.; Lee, S. Kelvin probe force microscopy and its application. *Surf. Sci. Rep.* **2011**, *66* (1), 1−27.
(34) Stolterfoht, M.; Wolff, C. M.; Amir, Y.; Paulke, A.; Perdigon-Toro, L.; Caprioglio, P.; Neher, D. Approaching the fill factor Shockley-Queisser limit in stable, dopant-free triple cation perovskite solar cells. *Energy Environ. Sci.* **2017**, *10* (6), 1530−1539.
(35) Xu, J.; Buin, A.; Ip, A. H.; Li, W.; Voznyy, O.; Comin, R.; Yuan, M.; Jeon, S.; Ning, Z.; McDowell, J. J.; Kanjanaboos, P.; Sun, J. P.; Lan, X.; Quan, L. N.; Kim, D. H.; Hill, I. G.; Maksymovych, P.; Sargent, E. H. Perovskite-fullerene hybrid materials suppress hysteresis in planar diodes. *Nat. Commun.* **2015**, *6*, 7081.
(36) Jia, T.; Sun, C.; Xu, R.; Chen, Z.; Yin, Q.; Jin, Y.; Yip, H.-L.; Huang, F.; Cao, Y. Naphthalene Diimide Based n-Type Conjugated Polymers as Efficient Cathode Interfacial Materials for Polymer and Perovskite Solar Cells. *ACS Appl. Mater. Interfaces* **2017**, *9* (41), 36070−36081.
(37) Wang, J.; Meng, F.; Li, R.; Chen, S.; Huang, X.; Xu, J.; Lin, X.; Chen, R.; Wu, H.; Wang, H.-L. Boosting Efficiency and Stability of Planar Inverted (FAPbI3)x(MAPbBr3)1−x Solar Cells via FAPbI3 and MAPbBr3 Crystal Powders. *Sol. RRL* **2020**, *4* (5), 2000091.
(38) Liu, C.; Zhang, L.; Li, Y.; Zhou, X.; She, S.; Wang, X.; Tian, Y.; Jen, A. K. Y.; Xu, B. Highly Stable and Efficient Perovskite Solar Cells with 22.0% Efficiency Based on Inorganic−Organic Dopant-Free Double Hole Transporting Layers. *Adv. Funct. Mater.* **2020**, *30* (28), 1908462.
(39) Shi, D.; Adinolfi, V.; Comin, R.; Yuan, M.; Alarousu, E.; Buin, A.; Chen, Y.; Hoogland, S.; Rothenberger, A.; Katsiev, K.; Losovyj, Y.;

https://doi.org/10.1021/jacs.1c02118
J. Am. Chem. Soc. 2021, 143, 7759−7768

Zhang, X.; Dowben, P. A.; Mohammed, O. F.; Sargent, E. H.; Bakr, O. M. Solar cells. Low trap-state density and long carrier diffusion in organolead trihalide perovskite single crystals. *Science* **2015**, *347* (6221), 519−22.
(40) Jinhua, L.; Qingde, Z.; Kaiyue, Z.; Dafa, C.; Haiping, X. Synthesis and Reactivity Studies of Irida-carbolong Complexes. *Acta Chimica. Sinica.* **2021**, *79* (1), 71−80.
(41) Zhuo, Q.; Lin, J.; Hua, Y.; Zhou, X.; Shao, Y.; Chen, S.; Chen, Z.; Zhu, J.; Zhang, H.; Xia, H. Multiyne chains chelating osmium via three metal-carbon σ bonds. *Nat. Commun.* **2017**, *8* (1), 1912.
(42) Dolomanov, O. V.; Bourhis, L. J.; Gildea, R. J.; Howard, J. A.; Puschmann, H. OLEX2: a complete structure solution, refinement and analysis program. *J. Appl. Crystallogr.* **2009**, *42* (2), 339−341.
(43) Sheldrick, G. M. SHELXT−Integrated space-group and crystal-structure determination. *Acta Crystallogr., Sect. A: Found. Adv.* **2015**, *71* (1), 3−8.
(44) Sheldrick, G. M. Crystal structure refinement with SHELXL. *Acta Crystallogr., Sect. C: Struct. Chem.* **2015**, *71* (1), 3−8.

https://doi.org/10.1021/jacs.1c02118
J. Am. Chem. Soc. 2021, 143, 7759−7768